# Guided Entry Performance of Low Ballistic Coefficient Vehicles at Mars

**Ian Meginnis, Zachary Putnam, Ian Clark, Robert Braun**
**Daniel Guggenheim School of Aerospace Engineering**
**Georgia Institute of Technology**
**270 Ferst Drive**
**Atlanta, GA 30302**
**404-894-7783**
**meginnis@gatech.edu**

**Gregg Barton**
**Charles Stark Draper Laboratory**
**17629 El Camino Real, Suite 470**
**Houston, TX 77058**
**gbarton@draper.com**

***Abstract*—Current Mars entry, descent, and landing technology is near its performance limit and is unable to land payloads on the surface that exceed approximately 1 metric ton. One option for increasing landed payload mass capability is decreasing the entry vehicle's hypersonic ballistic coefficient. A lower ballistic coefficient vehicle decelerates higher in the atmosphere, providing additional timeline and altitude margin necessary for heavier payloads. This study analyzed the guided entry performance of concept low ballistic coefficient vehicles at Mars. A terminal point controller guidance algorithm was used to provide precision targeting capability. Accuracy at parachute deploy, peak deceleration, peak heat rate, and integrated heat load were assessed and compared to a traditional vehicle to determine the effects of lowering the vehicle ballistic coefficient on entry performance. Results from this study suggest that while accuracy at parachute deploy degrades with decreasing ballistic coefficient, accuracy and other performance metrics remain within reasonable bounds for ballistic coefficients as low as 1 kg/m$^2$. As such, this investigation demonstrates that from a performance standpoint, guided entry vehicles with large diameters may be feasible at Mars.**

### TABLE OF CONTENTS



## 1. INTRODUCTION

The largest guided entry mission to Mars is the Mars Science Laboratory (MSL). MSL's base diameter is constrained by the present-day launch vehicle fairing diameter; because of this, MSL is approaching the limit on the maximum landed mass at Mars using Viking-derived systems, with a landed mass of 900 kg. With current entry methods, future higher landed mass systems would decelerate lower in the atmosphere, decreasing the timeline for which landing systems could be deployed and become effective. MSL has already reached the capabilities of present-day landing systems. [1] Studies for missions involving higher mass vehicles, including advanced robotic missions, human-precursor missions, and later human exploration missions, have considered using lower ballistic coefficient (β) systems to increase landed mass. [2] Lower β systems experience most of their energy dissipation at higher altitudes, increasing the landing sequence timeline.

The ballistic coefficient is defined in Equation 1:

$$\beta = \frac{m}{C_D * A} \quad (1)$$

where, m is the mass, $C_D$ is the drag coefficient, and A is the aerodynamic reference area.

Of the three ways to reduce the ballistic coefficient (decrease mass, increase drag coefficient, and/or increase aerodynamic reference area), the latter method is typically selected: the aeroshell diameter is increased. For traditional systems, the maximum aeroshell diameter is limited by the launch vehicle payload fairing. MSL, for example, is limited to 4.5 m. [1] To circumvent the payload fairing restriction, larger mass vehicles could use rigid, semi-rigid, or inflatable deployable decelerators to reduce their ballistic coefficient. [3] Figure 1 shows possible deployable decelerator options, which are discussed in greater detail in Reference [4].

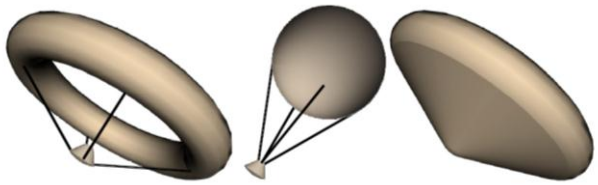

**Figure 1 – Trailing torus (left), trailing sphere (center), and clamped torus (right) hypersonic inflatable aerodynamic decelerators [4]**

Figure 2 illustrates how entry trajectories vary with ballistic coefficient for the four guided entry cases analyzed in this study. The figure shows that lower β systems spend more time at higher altitudes. This is a concern because atmospheric uncertainties increase with altitude. This is especially true at Mars, where atmospheric uncertainties are large.

978-1-4577-0557-1/12/$26.00 ©2012 IEEE

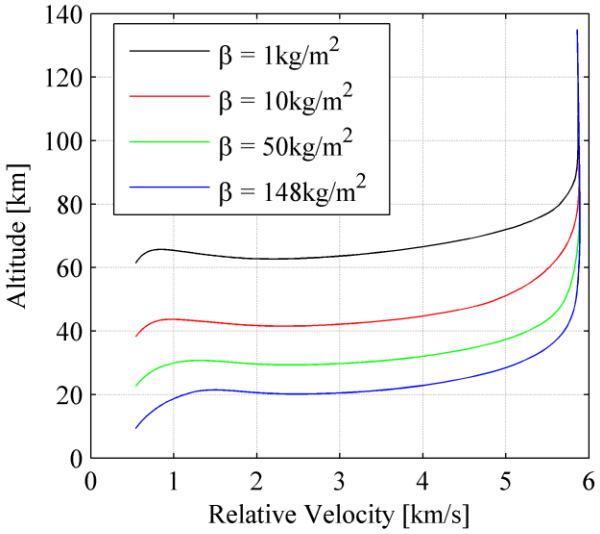


**Figure 2 – Trajectory comparison for β = 1 kg/m$^2$, 10kg/m$^2$, 50kg/m$^2$, and 148 kg/m$^2$**

This study quantified the relationship between ballistic coefficient and target miss distance using the traditional approach to guided entry at Mars. Nominal and dispersed trajectories were analyzed to determine the sensitivities between ballistic coefficient and miss distance. The terminal point controller guidance algorithm that is used by MSL was approximated in this study.

The traditional approach to guided entry at Mars uses bank angle modulation. This study assumed that it was possible to use this form of control to guide low ballistic coefficient vehicles to a specified target. This assumption made it possible to compare the entry trajectory of a baseline MSL-like, traditional vehicle with that of lower ballistic coefficient vehicles. This investigation did not assess whether traditional control methods of bank modulation, such as reaction control thrusters, are compatible with the large aeroshells associated with low ballistic coefficient vehicles.

## 2. APPROACH

This study analyzed the performance of several different vehicles at Mars. The properties for each vehicle were equivalent and similar to MSL, with the exception of the aerodynamic reference area. A three-degree-of-freedom trajectory simulation was integrated with a terminal point controller precision guidance algorithm that was derived from the Apollo Final Phase algorithm. A nominal set of target conditions was developed for each vehicle to create nominal trajectories. Each trajectory's termination condition occurred at a planet-relative velocity of 540 m/s, the approximate MSL parachute deployment velocity. [5] A Monte Carlo analysis was performed. The primary metric of interest in this study was target miss distance. Other parameters of interest included peak heat rate, peak deceleration, integrated heat load, and the vehicle state at parachute deployment.

*Trajectory Simulation*

The three-degree-of-freedom simulation used in this study was developed by the Space Systems Design Laboratory at the Georgia Institute of Technology. The equations of motion governing entry were integrated with a fixed time-step, fourth-order Runge-Kutta method. The trajectories were integrated at a frequency of 10 Hz. The simulation was written in Matlab but was autocoded and compiled into the C programming language to improve run-time speed.

*Vehicle Models*—The vehicles analyzed in this study span ballistic coefficients between 1 kg/m$^2$ and 148 kg/m$^2$. The latter ballistic coefficient represents a traditional, MSL-like aeroshell. The vehicle mass and aerodynamics were based on properties from MSL, which are defined in Table 1. The hypersonic drag coefficient for a 70 deg sphere cone shape at Mach 25 was used to calculate each reference area.

Hypersonic aerodynamics for the vehicles in this study were interpolated using a table-lookup with Mach number. The table was generated using the Configuration Based Aerodynamics (CBAERO) software package with a 70 deg sphere cone. CBAERO is a panel method aero-thermodynamics tool that uses Modified Newtonian flow to compute aerodynamic coefficients of complex geometries. [6] A trim angle of attack of -15.75 deg was used to produce a hypersonic lift-to-drag ratio of 0.24.

**Table 1 – Vehicle Properties**

| Parameter | Value |
|---|---|
| Mass | 3300 kg |
| Vehicle Shape | 70 deg sphere cone |
| Aerodynamic Reference Diameter | 4.5 m |
| Hypersonic L/D | 0.24 [5] |
| Trim Angle of Attack | -15.75 deg |

*Environment Models*—Mars was modeled as an ellipsoid using the planet's equatorial and polar radii. Gravity was modeled as an inverse square magnitude with $J_2$ effects. The Mars atmosphere was modeled with a table of density, temperature, and wind as functions of altitude. The table was generated using Mars - Global Reference Atmosphere Model (GRAM) 2010. [7]

In addition to generating a nominal Mars atmosphere, Mars-GRAM can also generate randomly dispersed atmospheres for Monte Carlo simulations. This capability was used to generate a set of 1000 dispersed atmospheres with which the different ballistic coefficient vehicles were tested. Mars-GRAM provided a density dispersion factor that was applied to the nominal density. A winds factor was also applied to the nominal winds.

Figure 3 shows a plot of the nominal density variation with altitude used in the Monte Carlo simulations. Near the entry altitude of 135 km, the dispersed density varied by as much

as ± 80 percent of the nominal density. At altitudes below 20 km, the density was much less dispersed, with a variation of approximately ± 5 percent of the nominal density. Figure 4 shows the variation in wind magnitude as a function of altitude used in the Monte Carlo simulations. Wind variations were largest between altitudes of 0 km to 20 km and 80 km to 110 km.

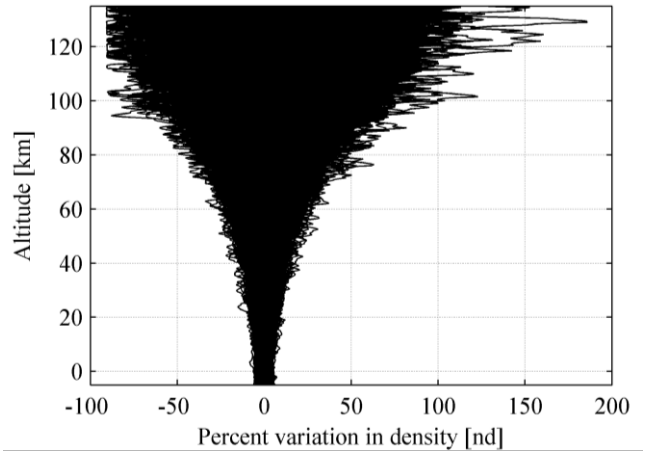


**Figure 3 – Mars-GRAM density variations**

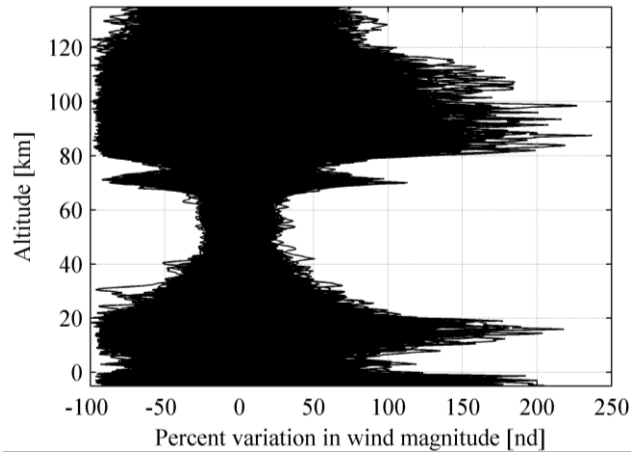


**Figure 4 – Mars-GRAM wind variations**

*Guidance, Navigation, and Control*

To provide the best approximation of MSL entry performance, an approximation of the MSL guidance algorithm was developed based on the Apollo Final Phase guidance algorithm and Reference [5]. No flight control algorithms were implemented, but a bank rate limiter was employed to approximate finite bank maneuvers. A rate limit of 20 deg/s was used [8]. Perfect navigation was assumed.

The developed guidance algorithm is composed of three distinct phases:

1. Pre-entry phase
2. Apollo Final Phase
3. Heading alignment phase

The first phase holds a preset bank angle until the vehicle reaches a sensed deceleration of 0.5 Earth g's, at which point the algorithm transitions to the Apollo Final Phase. The Apollo Final Phase is used to steer out downrange errors while managing crossrange errors. The algorithm transitions to the heading alignment phase at a velocity of 1100 m/s. The heading alignment phase is used to maintain altitude while steering out remaining crossrange errors.

Guidance execution terminates at parachute deployment at 540 m/s planet-relative velocity. This termination condition was selected to simplify the target miss distance calculation. Uncertainties in the entry sequence can be difficult to model after parachute deploy.

*Apollo Final Phase*—The Apollo Final Phase algorithm is a terminal point controller that determines bank commands based state errors relative to a pre-generated reference trajectory [9]. The Final Phase decouples longitudinal and lateral steering. The terminal point controller is used to null the downrange error, while crossrange error is managed via periodic bank reversals.

Bank commands are generated during Final Phase according to the following equation:

$$\left(\frac{L}{D}\right)_{cmd} = \left(\frac{L}{D}\right)_{ref} + \frac{4\left(r_{to\ go} - X_{to\ go}\right)}{F_3} \tag{2}$$

where, $(L/D)_{cmd}$ is the commanded vertical lift-to-drag ratio, $(L/D)_{ref}$ is the constant reference trajectory L/D command, $r_{togo}$ is the range to the target, $x_{togo}$ is the predicted vehicle flight range during the Final Phase, and $F_3$ is the partial derivative of range with respect to L/D and is stored in a table. The predicted vehicle flight range is computed from:

$$x_{togo} = x_{ref}(V) + F_2(V)\left(\dot{h} - \dot{h}_{ref}(V)\right) + F_1(V)\left(D - D_{ref}(V)\right) \tag{3}$$

where reference values for the drag acceleration, D, and altitude rate, $\dot{h}$, are stored in the reference trajectory as functions of velocity. The reference gains $F_1$ and $F_2$ are the partials of range with respect to drag acceleration and altitude rate, respectively.

The bank command is then calculated from:

$$\phi_{cmd} = \cos^{-1}\left(\frac{(L/D)_{cmd}}{(L/D)_{nom}}\right) \tag{4}$$

where, $\varphi_{cmd}$ is the bank command and $(L/D)_{nom}$ is the vehicle's nominal lift-to-drag ratio.

The lateral channel periodically commands bank reversals to manage crossrange error during entry. Guidance computes the estimated crossrange error each cycle and determines the crossrange error limit as a function of velocity. If the crossrange error exceeds the limit, a bank reversal is

commanded. The crossrange limits decrease with the square of the velocity to ensure that the allowable errors decrease with decreasing control authority. For velocities above 3 km/s, the corridor width is halved to force an early bank reversal in most trajectories.

*Heading Alignment Phase*—The heading alignment phase begins at a velocity of 1100 m/s. The heading alignment phase's goals are to null the crossrange error and maintain altitude for parachute deploy. Downrange errors are completely neglected during this phase, highlighting the importance of altitude maintenance over accuracy for Mars missions to date. Bank commands are generated from the simple equation:

$$\phi_{cmd} = -\mathrm{K} \cdot \mathrm{atan}\left(\frac{\lambda}{\theta}\right) \quad (5)$$

where λ is the current heading error, θ is the current range to target, and K is a proportional gain (set to 100). During heading alignment, the bank command is limited to ± 30 deg to maintain altitude at parachute deploy.

*Final Phase Reference Trajectory Design*—New reference trajectories were generated for each vehicle concept in this study. This process was modified from the original formulation that is described in Reference [9] to include Mach-dependent vehicle aerodynamics and bank profile. Initial conditions for the reference trajectory were selected to match the expected vehicle state at Final Phase transition. The reference bank profile was chosen to provide the best overall accuracy at parachute deploy.

The reference trajectory is generated by first integrating simplified entry equations of motion from the given initial state to the desired terminal state, 540 m/s in this study, using a set of reference bank commands. The simplified equations of motion assume a non-rotating spherical planet. Then, the adjoint equations are integrated backwards in time from the terminal point to generate the reference control gains. This data, including the reference commands, is then compiled into a single table as a function of velocity for use in the guidance algorithm.

The type of bank angle profile developed in Reference [5] was used for this study. The profile is specified by three bank angles and two velocities. The early bank angle is used for velocities above 6 km/s. Between 2.5 km/s and 6 km/s, the reference bank command is linearly interpolated between the early bank angle and the late bank angle. Between 2.5 km/s and 1.1 km/s (the starting velocity for the heading alignment phase), the late bank angle is used. Velocities below 1.1 km/s use a reference bank angle of 15 deg. This section of the reference command is only used during reference trajectory generation and is not included in the reference trajectory that is used by the Final Phase. This ensures that the reference ranges in the reference trajectory are consistent throughout the trajectory.

MSL guidance uses an early bank angle near 75 deg and a late bank angle near 45 deg. [5] This type of bank angle profile is well-suited to Mars entry: the vehicle dives into the thicker atmosphere more quickly early in the trajectory and then slowly transitions to a more lift-up orientation to maintain altitude at parachute deploy.

For this study, early and late bank angles for the baseline vehicle were adjusted to maximize the size of the vehicle's range capability relative to a maximum miss distance of 10 km at parachute deploy, using Reference [5] as a starting point. Figure 5 shows the selected reference command as a function of velocity for the baseline vehicle: an early bank angle of 70 deg and a late bank angle of 55 deg.

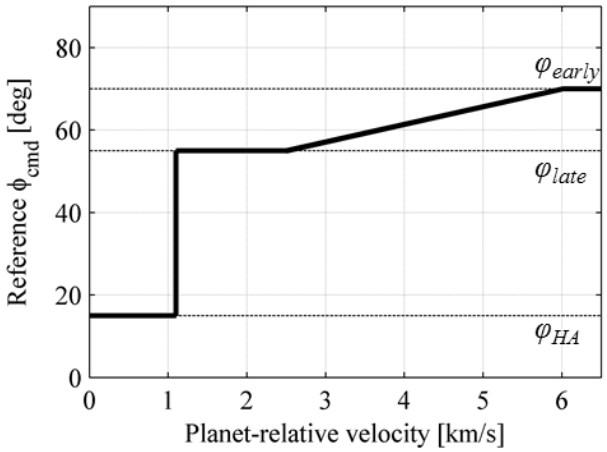


**Figure 5 – Reference bank profile for the baseline vehicle**

Figure 6 illustrates how reference bank profiles were selected for this study. The miss distance as a function of target longitude is shown for a ballistic coefficient of 50 kg/m$^2$. A late bank angle of 50 deg was used, and curves are shown for three early bank angles. In this case, an early bank angle of 55 deg provided the largest acceptable target longitude range capability with respect to a 10 km miss distance limit.

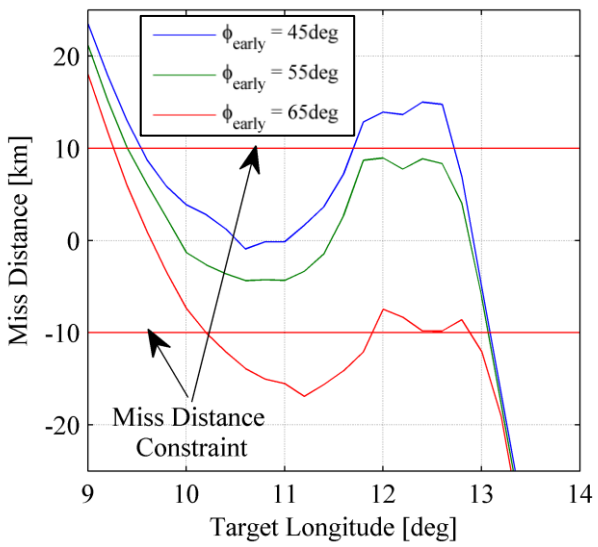


**Figure 6 – Miss distance profile for late bank angle of 50 deg and vehicle β = 50 kg/m$^2$**

The reference early and late bank angles for the four ballistic coefficient systems analyzed in this study are given in Table 2. The data shows that the range capability footprint improves for lower β vehicles when a more lift-up reference command profile is used.

**Table 2 – Nominal Bank Angle Profiles**

| β [kg/m$^2$] | Early Bank [deg] | Late Bank [deg] |
|---|---|---|
| 1 | 45 | 20 |
| 10 | 55 | 40 |
| 50 | 55 | 50 |
| 148 (baseline) | 70 | 55 |

*Monte Carlo Design Uncertainties*

There are many uncertainties associated with a spacecraft entering the Mars atmosphere. These uncertainties impact the ability of the vehicle to reach its intended target. Monte Carlo simulations were performed in this study to analyze the performance of the various ballistic coefficient systems when subject to day-of-flight uncertainties. Uncertainties analyzed in this study included vehicle aerodynamics, atmospheric parameters, vehicle mass, and entry state. Table A-1 in the Appendix shows the nominal value, dispersion type, and variation limits (3σ or minimum/maximum) for each dispersed parameter [8] [10]. These dispersions were randomly applied to the nominal values to generate a set of 1000 entry states.

*Metrics of Interest*

Several metrics were used to assess the performance of the different ballistic coefficient systems in this study. These metrics included miss distance, peak sensed deceleration, peak heat rate, integrated heat load, and vehicle state at parachute deploy. The miss distance was calculated by comparing the final latitude and longitude with the target latitude and longitude. The peak heat rate was calculated for the stagnation point using the Sutton-Graves equation. This relation does not include radiative heating. While radiative heating at Mars is typically not large, this may not be the case for larger vehicles, such as the concepts analyzed in this study. Peak heat rate and integrated heat load were calculated based on an effective nose radius of 1 m for all vehicles in this study.

## 3. Results: Nominal Trajectories

Nominal entry trajectories were calculated for the baseline entry vehicle and three ballistic coefficient variations of 50, 10, and 1 kg/m$^2$. All trajectories used the same entry interface state, which was based on Reference [5] (see Table 3). Target longitudes were selected to be in the center of the vehicle's downrange capability and are given in Table 4.

**Table 3 – Entry Interface State**

| Parameter | Value |
|---|---|
| Geodetic altitude | 135 km [5] |
| Geodetic latitude | 0 deg |
| Longitude | 0 deg |
| Inertial velocity magnitude | 6.1 km/s [5] |
| Inertial geodetic flight-path angle | -15.5 deg [5] |
| Inertial geodetic azimuth angle | 90 deg |

**Table 4 – Nominal Targeting Conditions**

| β [kg/m$^2$] | Target Latitude [deg] | Target Longitude [deg, positive East] |
|---|---|---|
| 1 | 0 | 7.69 |
| 10 | 0 | 9.77 |
| 50 | 0 | 11.2 |
| 148 (baseline) | 0 | 12.5 |

Figure 7 shows the baseline vehicle's entry trajectory. Deceleration primarily occurs near 20 km, with a peak deceleration of approximately 10 Earth g's. The trajectory terminates at the parachute deploy condition of 540 m/s. The flight-path angle at this point is about -17 deg, indicating that the vehicle has just barely begun its gravity turn at this point.

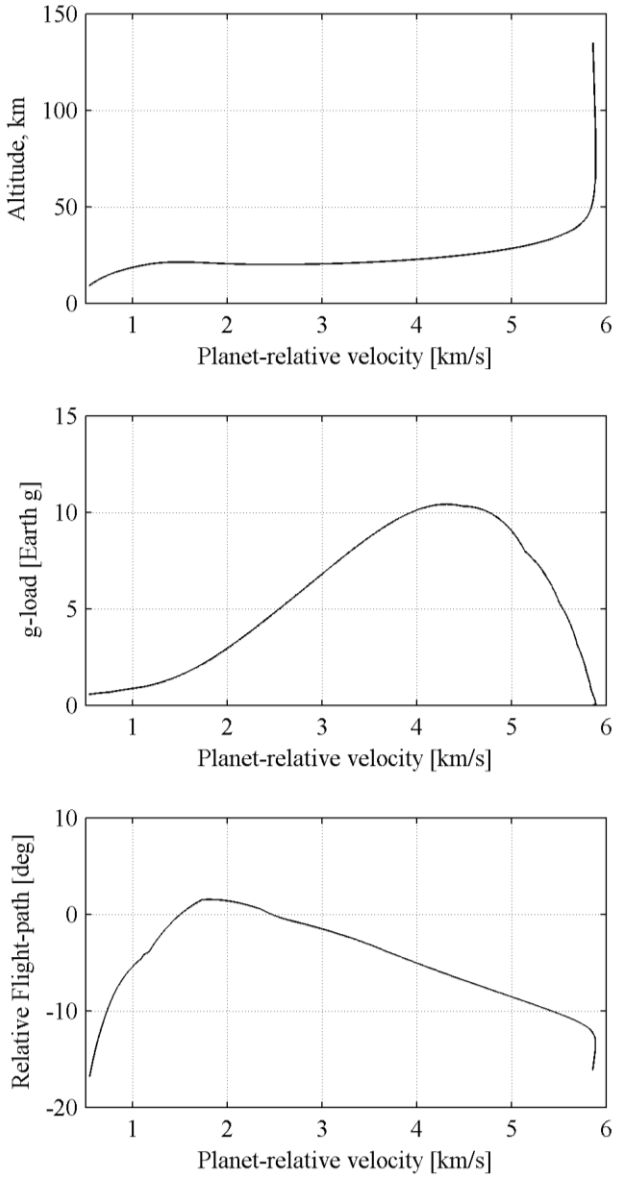


**Figure 7 – Baseline vehicle nominal entry trajectory**

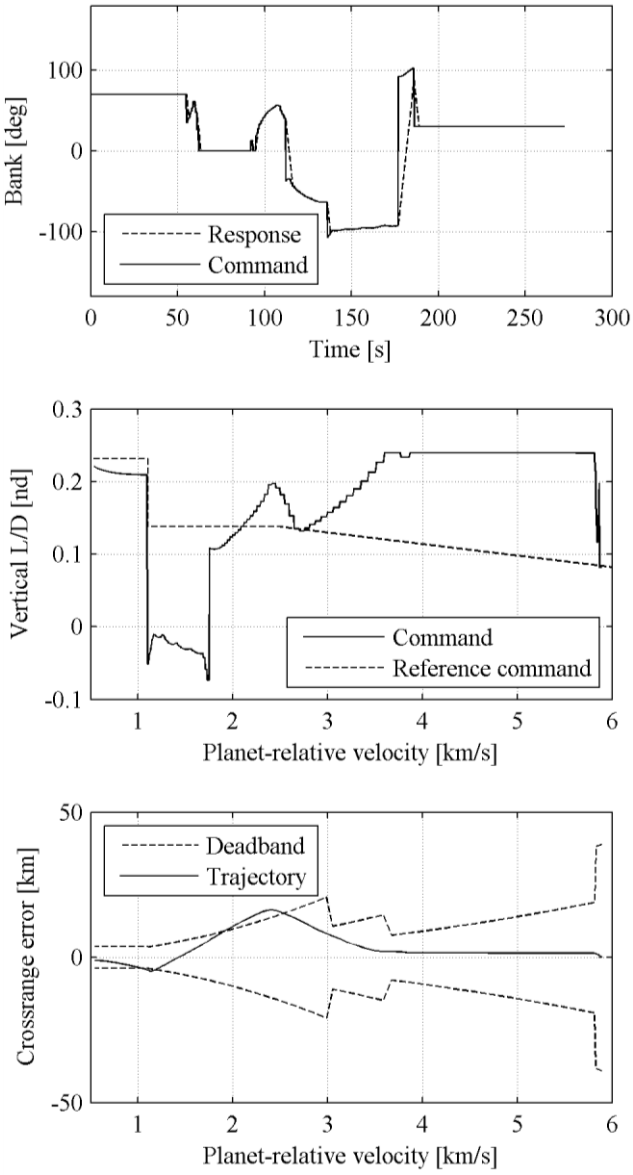


**Figure 8 – Baseline vehicle nominal entry guidance commands**

Figure 8 shows the guidance commands associated with the nominal baseline trajectory. While the bank command does not track the reference Final Phase command very closely, the miss distance at parachute deploy is small (2.86 km). The difference in commands exists because the nominal trajectory was not selected to match the design target range of the reference trajectory, as discussed in the previous section. There is significant lift-up saturation near peak deceleration, explaining why the peak deceleration is significantly lower than shown in Reference [5]. The jump in the guidance command near 140 seconds is due to the switch in the targeting logic from predicting target position at arrival to chasing the target. The vehicle performs two bank reversals prior to the initiation of the heading alignment phase. The heading alignment phase is able to remove most of the remaining crossrange error prior to parachute deploy.

Figure 9 shows the nominal trajectories for all four ballistic coefficient vehicles. The trend among the trajectories is as expected: lower ballistic coefficient systems decelerate significantly higher in the atmosphere and have a similarly higher altitude at parachute deploy. However, the low-β, high-altitude deceleration results in increased peak deceleration and a slightly less steep flight-path angle at deploy.

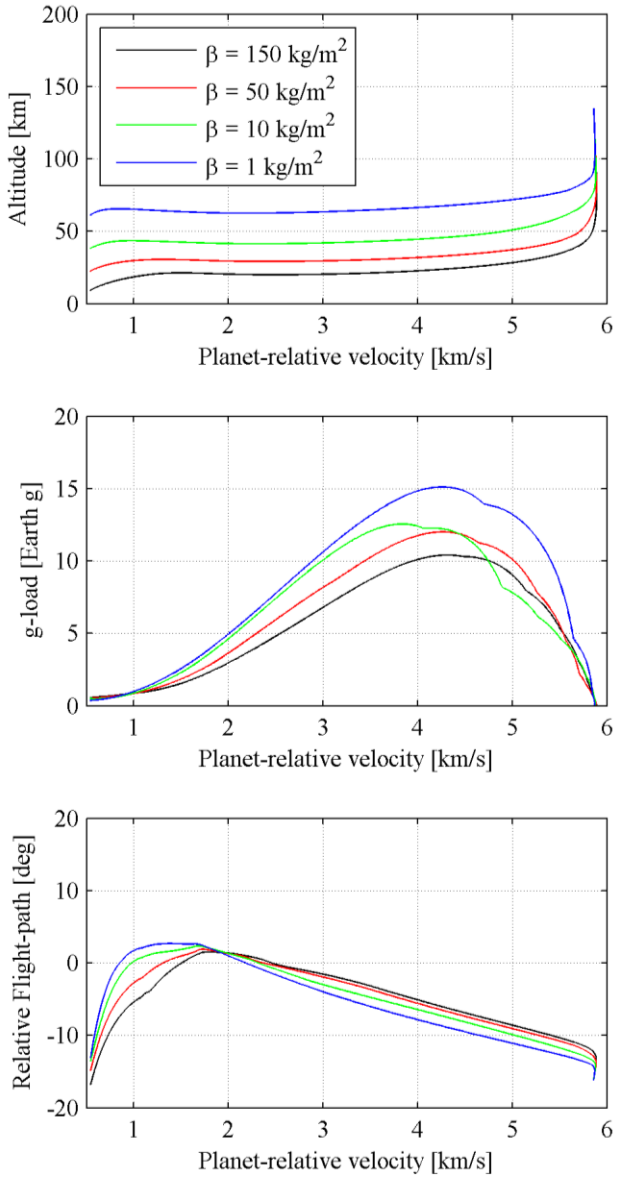


**Figure 9 – Nominal trajectories for several ballistic coefficient systems**

Guidance commands for these trajectories are shown in Figure 10. All of the trajectories exhibit a significant amount of lift-up saturation early on in the trajectory, near peak deceleration. This is a result of the targeting methodology used for this study: target downranges were selected to center the target within the vehicle's range capability footprint, which created a range trajectory that exceeded the reference trajectory's range trajectory. This resulted in more lift-up bank angles throughout the entry. All of the bank command histories exhibit similar features but at different times because of the different flight times for each vehicle. All vehicles except the $\beta$ = 1 kg/m$^2$ case perform two bank reversals prior to heading alignment initiation.

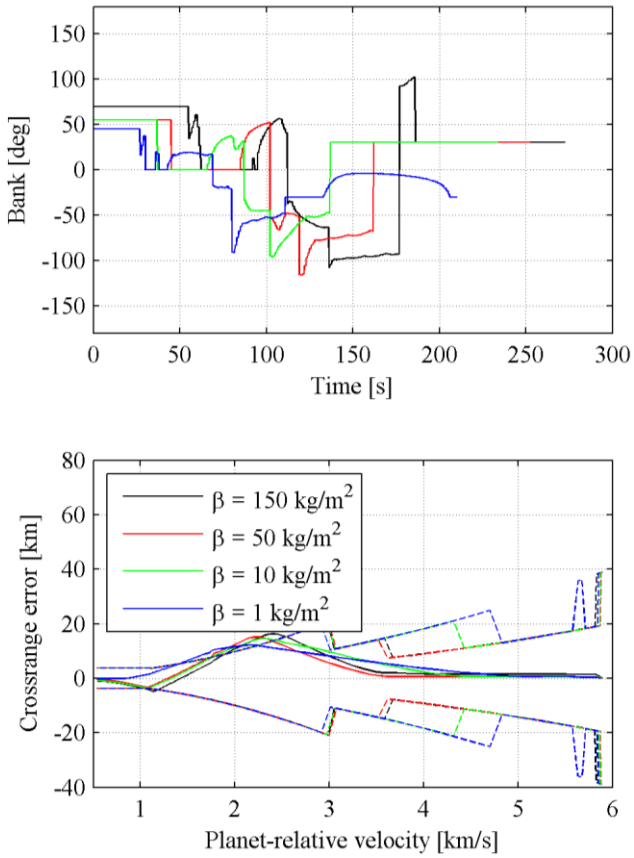


**Figure 10 – Guidance commands for nominal trajectories for several ballistic coefficient systems**

## 4. RESULTS: DISPERSED TRAJECTORIES

*Monte Carlo Results with All Dispersions*

1000-sample Monte Carlo simulations were performed for each ballistic coefficient with dispersions in all of the parameters listed Table A-1. Results from these simulations are summarized in Table A-2. As the ballistic coefficient decreased, the standard deviation of the miss distance increased. The standard deviations of the miss distances for $\beta$ = 148 kg/m$^2$ and 1 kg/m$^2$ were 1.43 km and 2.37 km, respectively. This trend is evident in Figure 11, showing the crossrange error as a function of the downrange error.

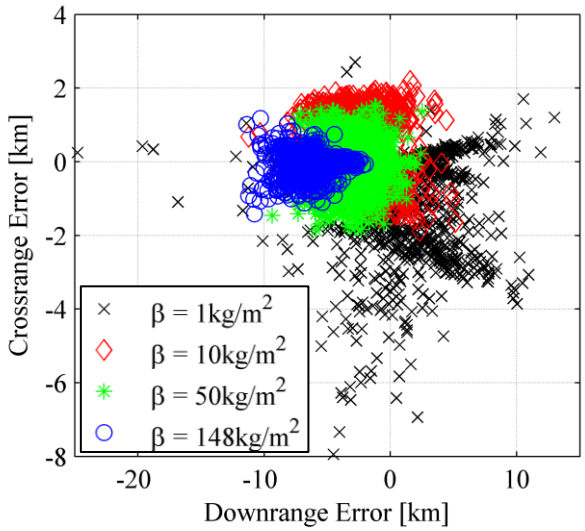


**Figure 11 – Crossrange and Downrange Error Monte Carlo Dispersions**

Although the variation of the target miss distance increased as the ballistic coefficient decreased, the target accuracies of all of the ballistic coefficient systems were still very good. Reference [5] cites a desired accuracy of 10 km at parachute deploy to accommodate a 25 km x 20 km landing ellipse requirement for MSL. Based on the Monte Carlo simulation, all of the ballistic coefficient systems in this study met or were close to the parachute deploy accuracy requirement. The worst-performing vehicle configuration, $\beta$ = 1 kg/m$^2$, had a mean miss distance of 3.38 km and a mean + 3$\sigma$ standard deviation of 10.5 km, nearly equal to the stated performance goals for MSL.

In addition to meeting the MSL targeting requirements, the lower ballistic coefficient cases performed better than the baseline vehicle case with respect to peak heat rate and integrated heat load. However, a single nose radius of 1 m was used for all of the ballistic coefficient systems, and the larger, lower ballistic coefficient vehicles may have large nose radii, depending on their configuration. The mean peak heat rates for $\beta$ = 1 kg/m$^2$ and $\beta$ = 148 kg/m$^2$ differed by almost a factor of ten. Additionally, the lower ballistic coefficient systems provided substantially more time for the landing sequence; the mean parachute deploy altitudes for $\beta$ = 1 kg/m$^2$ and $\beta$ = 148 kg/m$^2$ were 61 km and 23 km, respectively. This is shown in Figure A-2(a). With these advantages, however, came higher peak decelerations for the lower ballistic coefficient systems. Figure A-1(d) shows that the mean peak deceleration for $\beta$ = 1 kg/m$^2$ was 17 Earth g's, while the mean peak deceleration for 148 kg/m$^2$ was just 10.5 Earth g's.

*Monte Carlo Results for Individual Dispersions*

Additional Monte Carlo simulations were performed to characterize the individual contributions to performance and final state uncertainty from the parameters listed in Table A-1. Four Monte Carlo simulations were performed for each ballistic coefficient, using uncertainties in only one of the following parameter groups: atmosphere density, atmosphere winds, aerodynamics, and entry state. Figure A-3 and Figure A-4 show the contributions of these uncertainties to the vehicle performance and final vehicle state, respectively. While this method does not address interaction effects across multiple uncertainty groups, it does provide a measure of the relative impact of the group on entry performance. The influence of mass uncertainty was not analyzed because it was negligible compared to the dispersion effects from the other parameters.

Figure A-3 and Figure A-4 show that lower-$\beta$ vehicles are more susceptible to uncertainties, regardless of the source. Aerodynamic uncertainties were the largest contributors to miss distance variation. Figure A-3 shows that density uncertainties played a much more important role than wind uncertainties in defining the variability of the miss distance. This explains why the miss distance uncertainty increased with decreasing ballistic coefficient. Smaller ballistic coefficient systems experienced most of their decelerations at higher altitudes, where density uncertainties were also higher. This behavior is overlaid with density uncertainty and wind uncertainty in Figure 12 and Figure 13, respectively. Although Figure 13 shows that wind uncertainties were greater at lower altitudes (where high-$\beta$ vehicles decelerate), these uncertainties' impacts were minimal compared to the impacts from density uncertainties.

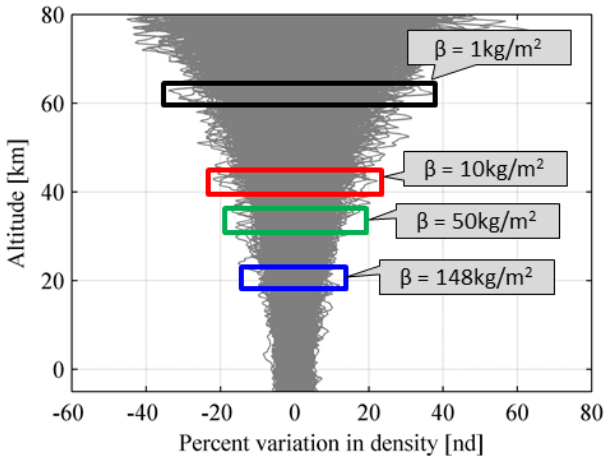


**Figure 12 – Primary altitudes of deceleration for various ballistic coefficient systems overlaid with density uncertainty**

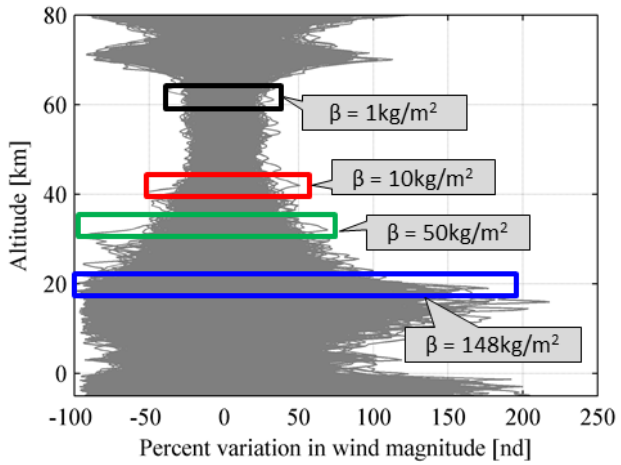


**Figure 13 – Primary altitudes of deceleration for various ballistic coefficient systems overlaid with wind uncertainty**

## 5. Conclusion

This analysis presented the guided entry performance of concept low ballistic coefficient vehicles at Mars. Various performance metrics, including target miss distance, were presented for several ballistic coefficient systems. Prior to this study, it was hypothesized that atmospheric uncertainties would have detrimental impacts to targeting accuracy as the ballistic coefficient decreased. Results from this study verified this trend, but showed that this effect is small in magnitude. This suggests that it is feasible, in terms of targeting requirements, to use guided entry vehicles at Mars with large diameter aeroshells.

Although the miss distance deviation increased with decreasing ballistic coefficient, the lower ballistic coefficient systems analyzed in this study were very close to meeting the performance goals for MSL. This suggests that the guidance algorithm used in this study is robust to atmospheric uncertainties, even for low ballistic coefficient systems. As the ballistic coefficient is reduced below 1 $kg/m^2$, it is expected that the targeting accuracy will degrade and fall outside of MSL's requirements.

## 6. Future Work

This study considered a single entry state for the different ballistic coefficient systems. In the future, it would be beneficial to incorporate different entry states into the analysis to determine the sensitivity of the results to varying entry states. Because radiative heating may be relevant for the smaller ballistic coefficient systems in this study, radiative heating should be included in future work when calculating heat rate and integrated heat load. Although very small ballistic coefficient systems may not be technologically feasible, it would be valuable to determine the ballistic coefficient at which a vehicle is unable to accurately reach an intended target. Finally, the trajectory simulation could be expanded to 6 degrees of freedom, and the vehicle aerodynamics could be improved. These changes would make the results more realistic.

## References

[1] Braun, R. D. and Manning, R. M., "Mars Exploration Entry, Descent and Landing Challenges", Journal of Spacecraft and Rockets, Vol. 44, No. 2, 2007.

[2] Dweyer Cianciolo, A., et al, "Entry, Descent and Landing Systems Analysis Study: Phase 1 Report," NASA-TM-2010-216720, July 2010.

[3] Adler, M. et al, "Draft Entry, Descent, and Landing Roadmap: Technology Area 09," NASA, November 2010.

[4] Clark, I.G., Braun, R.D., Theisinger, J.T., and Wells, G.W., "An Evaluation of Ballute Entry Systems for Lunar Missions," AIAA Atmospheric Flight Mechanics Conference, Aug. 2006.

[5] Mendeck, G. F., Craig, L, E., "Entry Guidance for the 2011 Mars Science Laboratory Mission," 2011 AIAA Atmospheric Flight Mechanics Conference, Aug. 2011.

[6] Kinney, D., "Aero-Thermodynamics for Conceptual Design," 2004 AIAA Aerospace Sciences Meeting and Exhibit, Paper 13382, Reno, NV, Jan. 2004.

[7] Justus, C. G., Johnson, D. L., "Mars Global Reference Atmospheric Model 2001 Version (Mars-GRAM 2001): Users Guide," April 2001.

[8] Striepe, S.,Way, D.W., Dwyer, A. M., and Balaram, J., "Mars Science Laboratory Simulations for Entry, Descent, and Landing," Journal of Spacecraft and Rockets, Vol. 43, No. 2, 2006, pp. 311–323.

[9] TRW, "The Apollo Entry Guidance: A Review of the Mathematical Development and Its Operational Characteristics," NASA T75-14618, December 1969.

[10] Steinfeldt, B. A., Grant, M. J., Braun, R. D., and Barton, G. H., "Guidance, Navigation, and Control System Performance Trades for Mars Pinpoint Landing," Journal of Spacecraft and Rockets, Vol. 47, No. 1, January-February 2010, pp. 188–198.

## BIOGRAPHIES

***Ian M. Meginnis*** *is currently a 2nd year Graduate Research Assistant in the Space Systems Design Laboratory at the Georgia Institute of Technology. He received a B.S. in Aerospace Engineering from Purdue University 2010. He has had previous work experience at NASA/Johnson Space Center. Mr. Meginnis is currently working on drag modulation as a form of hypersonic control for entry vehicles. He is co-advised by Dr. Robert Braun and Dr. Ian Clark.*

***Zachary R. Putnam*** *is a doctoral student in aerospace engineering in the Space Systems Design Lab at the Georgia Institute of Technology. His research focuses on guidance and control systems and mission design for aeroassist vehicles. He was previously a member of the technical staff at the Charles Stark Draper Laboratory, where he supported development of the Orion entry guidance system. Mr. Putnam received his B.S. and M.S. in Aerospace Engineering from the Georgia Institute of Technology.*

***Ian G. Clark*** *is a visiting assistant professor at the Georgia Institute of Technology and an employee of the Jet Propulsion Laboratory. He received his PhD from the Georgia Institute of Technology, where he also received his B.S. and M.S. Dr. Clark's current research involves developing and maturing IADs for use during atmospheric entry. As part of this research, Dr. Clark has worked on conceptual IAD system design, entry flight mechanics trades, and the development of fluid- structure interaction codes capable of predicting the behavior of flexible decelerators.*

***Robert D. Braun*** *is the David and Andrew Lewis Professor of Space Technology in the Daniel Guggenheim School of Aerospace Engineering at the Georgia Institute of Technology. As Director of Georgia Tech's Space Systems Design Laboratory, he leads a research program focused on the design of advanced flight systems and technologies for planetary exploration. He is responsible for undergraduate and graduate level instruction in the areas of space systems design, astrodynamics, and planetary entry. He served as NASA's Chief Technologist in 2010 and 2011. Prior to coming to Georgia Tech, he served on the technical staff of the NASA Langley Research Center, where he contributed to the design, development, test, and operation of several robotic space flight systems. Dr. Braun is an AIAA Fellow and holds a B.S. in Aerospace Engineering from Penn State University, a M.S. in Astronautics from George Washington University, and a Ph.D. in Aeronautics and Astronautics from Stanford University.*

***Gregg H. Barton*** *is a Group Leader for Mission Design of Earth, Moon, and Mars GN&C systems at the Houston office of the Charles Stark Draper Laboratory. He is the capability lead for skip entry guidance technologies for Earth return vehicles.*

# APPENDIX A

**Table A-1 – Monte Carlo Dispersions**

| Parameter | Nominal | Distribution | Deviation, 3σ or min/max |
|---|---|---|---|
| Entry Mass[8] | 3300 kg | Gaussian | 3.0 kg |
| Axial-Force Coefficient Multiplier [8] | 1.0 | Gaussian | 3% |
| Normal-Force Coefficient Multiplier [8] | 1.0 | Gaussian | 5% |
| Trim Angle of Attack [8] | -15.75 deg | Gaussian | 2.0 |
| Inertial Entry Flight-Path Angle | -15.5 deg | Gaussian | 0.050 deg |
| Entry Latitude | 0 deg | Gaussian | 0.100 deg |
| Entry Longitude | 0 deg | Gaussian | 0.100 deg |
| Entry Azimuth | 90 deg | Gaussian | 0.005 deg |
| Inertial Entry Velocity Magnitude | 6100 m/s | Gaussian | 2.0 m/s |
| Entry Altitude | 135 km | Gaussian | 2.5 km |
| Atmosphere Dust Opacity (Dust Tau) | 0.45 | Uniform | 0.1 / 0.9 |

**Table A-2a – Monte Carlo Statistics with All Dispersions**

| | Mean | | | | Standard Deviation | | | |
|---|---|---|---|---|---|---|---|---|
| | Ballistic Coefficient [kg/m$^2$] | | | | Ballistic Coefficient [kg/m$^2$] | | | |
| **Parameter** | **1** | **10** | **50** | **148** | **1** | **10** | **50** | **148** |
| Miss Distance [km] | 3.38 | 3.00 | 2.77 | 5.92 | 2.37 | 1.60 | 1.46 | 1.43 |
| Peak Sensed Deceleration [Earth g's] | 17.0 | 12.6 | 12.1 | 10.5 | 1.16 | 0.54 | 0.32 | 0.23 |
| Peak Heat Rate (convective) [W/cm$^2$] | 7.88 | 20.4 | 46.7 | 77.4 | 0.28 | 0.53 | 0.78 | 1.1 |
| Integrated Heat Load [J/cm$^2$] | 229 | 836 | 1959 | 3529 | 3.31 | 7.51 | 15.5 | 25.5 |
| Deploy Altitude [km] | 61.1 | 38.9 | 23.1 | 10.0 | 1.80 | 0.52 | 0.37 | 0.34 |
| Deploy Inertial Flight-Path Angle [deg] | -7.72 | -7.45 | -8.40 | -9.53 | 0.61 | 0.43 | 0.41 | 0.43 |
| Deploy Dynamic Pressure [Pa] | 3.58 | 43.4 | 232 | 737 | 0.32 | 1.69 | 6.01 | 21.4 |

**Table A-2b – Monte Carlo Statistics with All Dispersions**

| | Minimum | | | | Maximum | | | |
|---|---|---|---|---|---|---|---|---|
| | Ballistic Coefficient [kg/m$^2$] | | | | Ballistic Coefficient [kg/m$^2$] | | | |
| **Parameter** | **1** | **10** | **50** | **148** | **1** | **10** | **50** | **148** |
| Miss Distance [km] | 0.01 | 0.10 | 0.03 | 1.87 | 23.4 | 10.6 | 8.93 | 10.8 |
| Peak Sensed Deceleration [Earth g's] | 13.3 | 10.9 | 11.1 | 9.78 | 20.9 | 14.5 | 13.1 | 11.2 |
| Peak Heat Rate (convective) [W/cm$^2$] | 6.93 | 18.8 | 44.4 | 74.5 | 8.89 | 21.9 | 49.0 | 81.2 |
| Integrated Heat Load [J/cm$^2$] | 217 | 813 | 1916 | 3453 | 238 | 859 | 2010. | 3624 |
| Deploy Altitude [km] | 56.5 | 36.8 | 21.3 | 8.82 | 65.3 | 40.3 | 24.3 | 10.9 |
| Deploy Inertial Flight-Path Angle [deg] | -10.0 | -8.80 | -9.94 | -11.0 | -5.78 | -6.08 | -7.03 | -8.14 |
| Deploy Dynamic Pressure [Pa] | 2.92 | 39.7 | 208 | 674 | 4.97 | 51.0 | 266 | 798 |

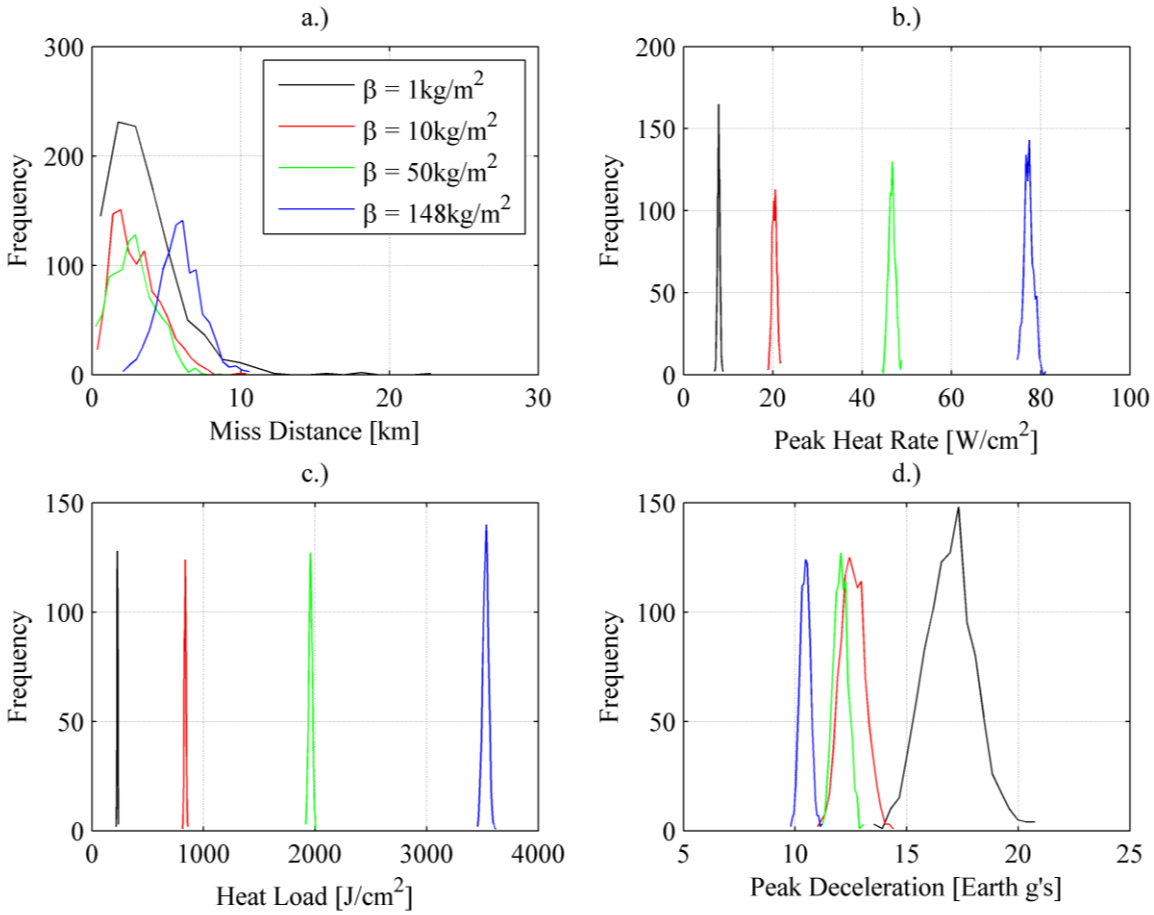


**Figure A-1 – Histogram of performance characteristics: a.) Miss Distance; b.) Peak Heat Rate; c.) Head Load; d.) Peak Deceleration**

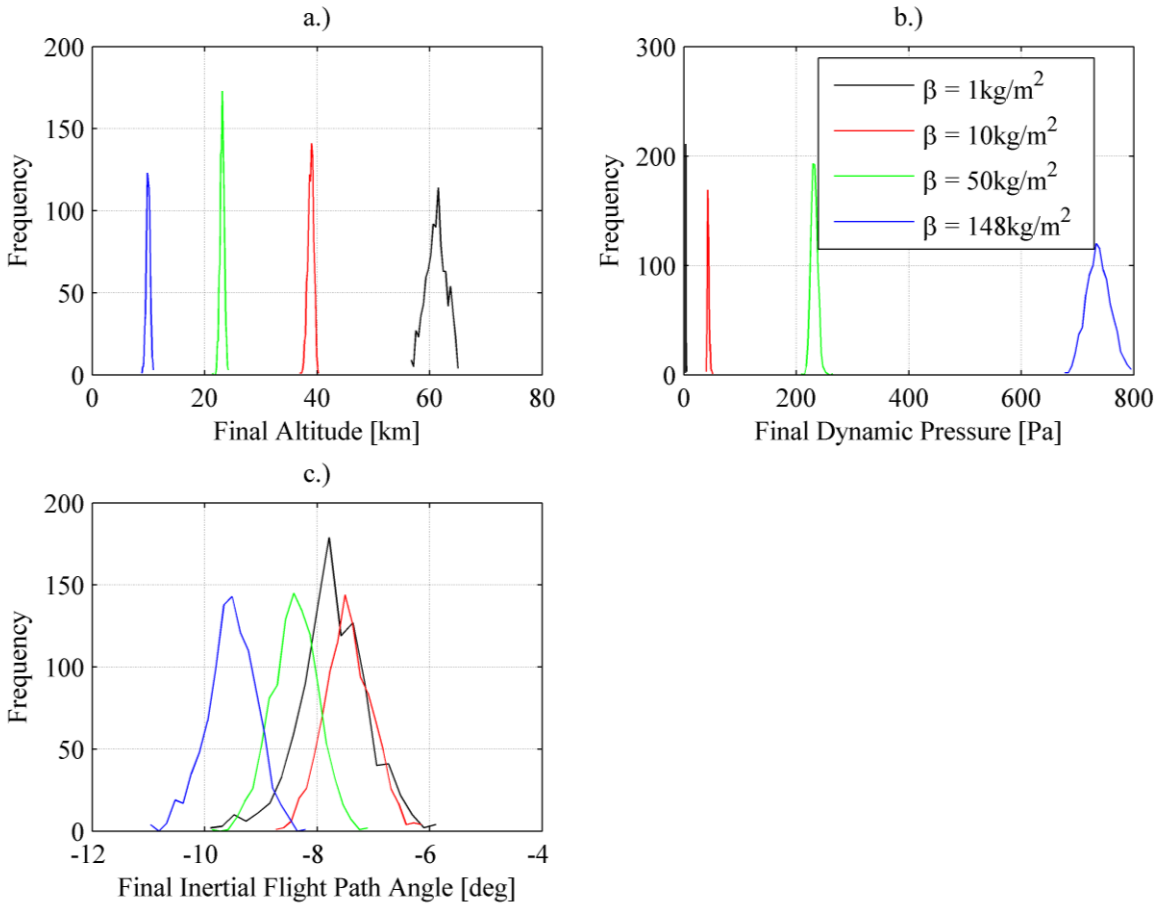


**Figure A-2 – Histogram of final state conditions: a.) Final Altitude; b.) Final Dynamic Pressure; c.) Final Inertial Flight-Path Angle**

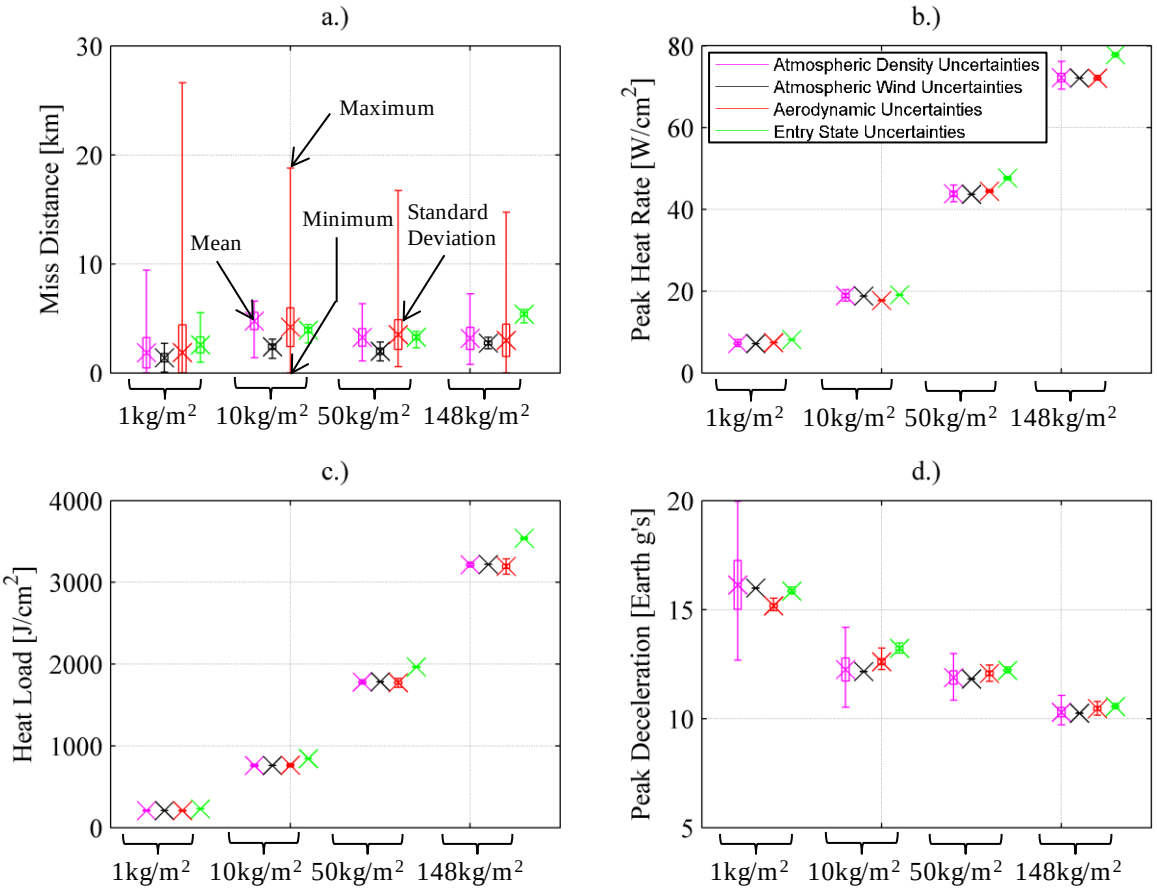


**Figure A-3 – Individual contributions to performance uncertainties: a.) Miss Distance; b.) Peak Heat Rate; c.) Head Load; d.) Peak Deceleration**

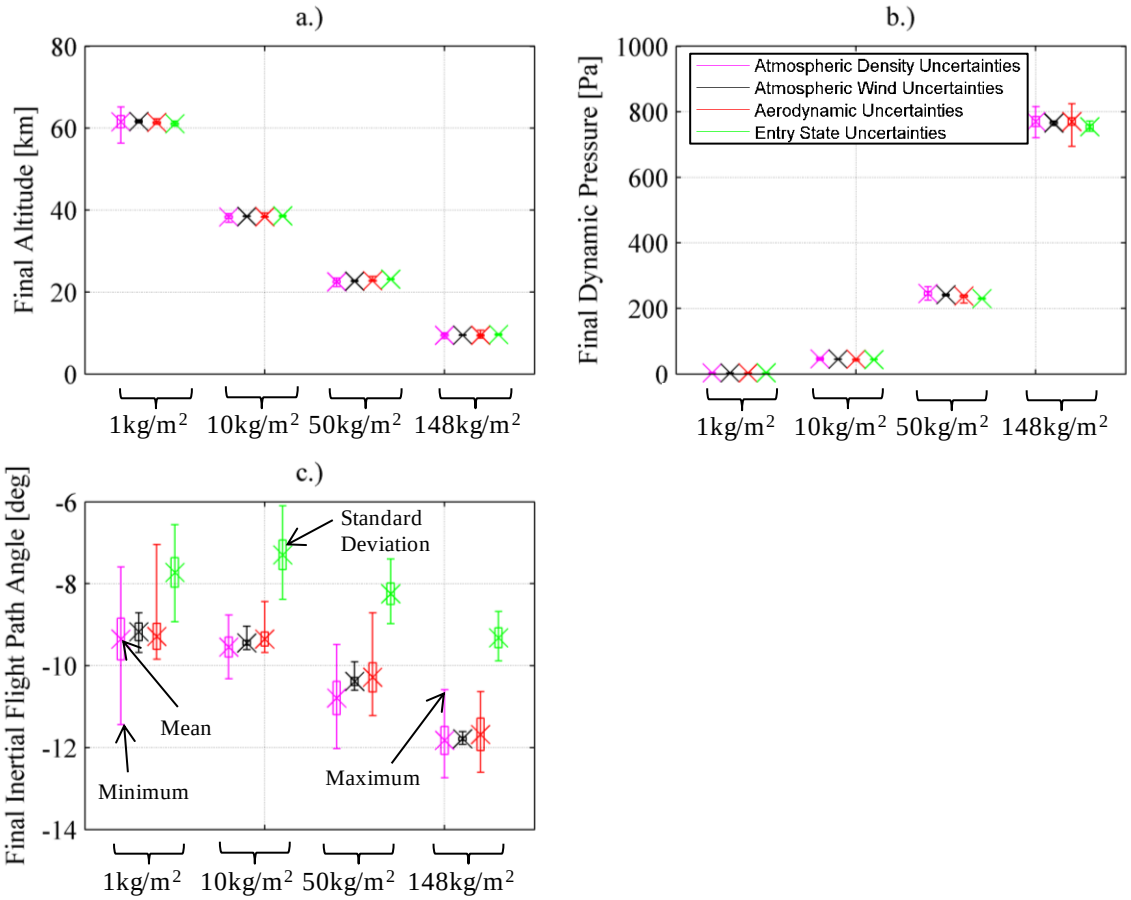


**Figure A-4 – Individual contributions to final state uncertainties: a.) Final Altitude; b.) Final Dynamic Pressure; c.) Final Inertial Flight-Path Angle**